USING BOREHOLE ELECTROSEISMIC MEASUREMENTS TO DETECT AND CHARACTERIZE FRACTURED (PERMEABLE) ZONES

Oleg V. Mikhailov

Earth Resources Laboratory
Department of Earth, Atmospheric, and Planetary Sciences
Massachusetts Institute of Technology
Cambridge, MA 02139

John H. Queen

Conoco, Inc.
Ponca City, OK 74603

M. Nafi Toksöz

Earth Resources Laboratory
Department of Earth, Atmospheric, and Planetary Sciences
Massachusetts Institute of Technology
Cambridge, MA 02139

ABSTRACT

We present a new type of field measurement capable of detecting and characterizing fractured (permeable) zones intersecting a borehole. The method is based on measuring electrical fields generated by a borehole Stoneley wave. In this paper, we describe the measurement technique, present field data, and propose a theoretical model, which correctly predicts amplitudes and phases of the electrical fields measured in the borehole experiment.

The theoretical model and the field data demonstrate that the measurements of the Stoneley-wave-induced electrical fields can yield information about the interconnected porosity, and possibly about the permeability of the formation around the borehole. We derive an estimate of the interconnected porosity from the field data, and show that

it correlates well with the density of fractures intersecting the borehole. Our results suggest that the borehole electroseismic method can be developed into a logging or a VSP tool, with possible applications in reservoir characterization.

INTRODUCTION

Electroseismic phenomena in fluid-saturated porous media provide geophysicists with a unique opportunity to detect a seismic-wave-generated flow of pore fluid with respect to the rock matrix. The term "electroseismic" describes phenomena in which a seismic wave induces an electrical field or causes radiation of an electromagnetic wave. Electroseismic phenomena take place in fluid-saturated porous rocks, because the pore fluid carries an excess electrical charge. When the charged pore fluid is forced to flow through the rock by pressure gradients within a seismic wave, a streaming electrical current is generated. This electrical current results in a charge separation, which induces an electrical field. Measuring this seismic-wave-induced electrical field allows detection of the fluid flow generated by the wave in the porous medium. In turn, detecting the fluid flow allows characterization of the fluid transport properties of the medium.

The potential ability of the electroseismic method to characterize the fluid transport properties of the subsurface can make it a useful tool for reservoir characterization. Theoretical studies (Haartsen and Pride, 1994; Haartsen, 1995) suggest that porosity and permeability contrasts in the subsurface can be detected by electroseismic measurements. Recent surface experiments (Thompson and Gist, 1993; Butler *et al.*, 1996; Mikhailov *et al.*, 1997) confirm that electroseismic signals from various interfaces in the subsurface can be detected. However, these studies also demonstrate that the penetration depth of the electroseismic method is limited by the exponential decay of the electrical field in a conductive earth. One way to overcome the penetration depth limitation is to place the detectors of the electrical field close to the formation of interest, i.e. to make electroseismic measurements in a borehole.

The idea of borehole electroseismic measurements has been around for quite a long time. However, only a few attempts of such measurements were made. Broding *et al.* 1963 made measurements with electrodes in a borehole and a seismic source away from a borehole (VSP-type measurements). Parkhomenko and Gaskarov (1971) placed electrodes in a borehole and excited seismic waves by striking the well-head (i.e., the seismic wave source was effectively in a borehole, thus these were logging type measurements). Both studies reported that the amplitude of the recorded electrical signals varied with lithology (higher amplitudes in limestones than in shales). However, they did not comment on how the detected electrical fields were generated, or what information about the formation could be deduced from the borehole electroseismic measurements. Therefore, the main goal of our work is not only to perform borehole electroseismic measurements, but also to identify different electroseismic phenomena in the field data, to develop a theoretical model explaining the observations, and to determine which properties of the formation can be derived from such measurements.

Borehole Electroseismic Field Measurements

In our borehole experiments we measured electrical fields generated by a Stoneley wave. When a borehole Stoneley wave travels past a fractured (permeable) zone, it induces a flow of the ion-carrying fluid within the fractures, thus creating a streaming electrical current from the borehole into the formation (Figure 1). The streaming electrical current results in a time-varying electrical charge separation, which locally induces an electrical field and also causes an electromagnetic wave radiation. Field data presented in this paper show both of these phenomena. Furthermore, the data demonstrate that a Stoneley wave induces stronger electrical fields in zones of higher fracture density, thus suggesting that the Stoneley-wave-induced electrical field can be used to detect and characterize fractured (permeable) zones around a borehole.

To determine what specific information about the fractured (permeable) zones can be derived from borehole electroseismic measurements, we developed a theoretical model and obtained an analytical solution for the amplitude and phase of the Stoneley-wave-induced electrical field. A quantitative comparison demonstrates that the analytical solution correctly predicts the amplitude and phase of the electrical fields observed in the experiment.

The analytical solution suggests that at a given frequency the amplitude of the Stoneley-wave-induced electrical field is proportional to the interconnected porosity of the formation around the borehole. We derive an estimate of the interconnected porosity from the field data, and demonstrate that it correlates with the density of fractures intersected by the borehole. Further analysis of the analytical solution suggests that if the borehole electroseismic measurements are performed over a wide frequency range, then the Biot critical frequency for the formation could possibly be determined, thus yielding information about the permeability. We suggest that the ability of the electroseismic method to determine the interconnected porosity, and possibly the permeability of a formation around the borehole, can make it a useful tool for reservoir characterization.

FIELD MEASUREMENT PROCEDURE AND NOISE REDUCTION PROCESSING

We conducted borehole electroseismic measurements in an open hole well in Hamilton, Massachusetts. Figure 2 shows a diagram of the experimental setup. During the experiments we generated a Stoneley wave at the top of the well, and recorded the pressure and electrical field generated by the wave as it traveled downward in the borehole. The Stoneley wave was generated by striking the wellhead with a sledge hammer. The pressure oscillations were recorded using a string of three hydrophones spaced one meter apart. The sensitivity of the hydrophones was $10mV/Pa$. The electrical fields were recorded as a potential difference between lead electrodes placed in an array in the borehole. We used 8-electrode arrays with electrode spacings of $0.5m$ and $1.0m$. To record signals measured by the hydrophones and the electrodes we used a data acquisition system with a dynamic range of $132dB$ and crosstalk between channels of less than $-100dB$.

In the experiments we made the pressure measurements and the electrical field measurements separately, to ensure that there was no crosstalk between channels. Since we were capable of only making either three hydrophone or four electrical measurements at a time, we had to consequently place the arrays at different depths in the borehole and repeat the source. Even though this was a disadvantage, we were able to demonstrate that the phenomena observed in the experiments were repeatable.

Nearby powerlines generated electrical noise in our data. We used remote referencing and powerline harmonic filters to reduce this noise. Details of the noise-reduction processing are given in Mikhailov *et al.* (1997). As a result of the processing, the signal-to-noise ratio in the electrical records was improved from 0.01 to about 5.0, thus allowing the data to be interpreted.

PRELIMINARY ANALYSIS OF THE FIELD DATA

The field experiments were conducted in an open-hole well drilled through fractured igneous rock. The top $140m$ of the well is in fractured granite, and below the depth of $140m$ is in fractured diorite (Figure 3). A $6m$ felsite dike intersects the well at a depth of $152m$. Video and borehole televiewer logs show numerous fractures and fractured zones along the entire depth interval of investigation. The average fracture density in granite is 4 per meter. Figures 3 and 4 show caliper, P-wave slowness, and conductivity logs. Slowness and conductivity highs correspond to fractured zones and isolated fractures.

Figure 5 presents the hydrophone pressure measurements. The down-going wave is the borehole Stoneley wave (event A-A). Its velocity varies from $1380m/s$ to $1450m/s$. Large fractures and fractured zones generate Stoneley wave reflections traveling upward. Figures 6 and 7 show the electrical measurements made with $0.5m$ and $1.0m$ electrode separation respectively. In these data the electrical field and the electromagnetic radiation induced by the Stoneley wave can be identified.

Electrical Field Induced by a Stoneley Wave

Figures 6 and 7 show an electrical signal, that arrives at the electrodes simultaneously with the Stoneley wave (event A-A). Figure 8 shows this signal enhanced by median-filtering. We suggest that the signal is the electrical field induced by the Stoneley wave forcing a flow of the ion-carrying pore fluid within the fractures (Figure 1).

Figure 9 shows the amplitude of the Stoneley-wave-induced electrical field normalized by the amplitude of the pressure oscillation in the wave. The amplitudes of the electrical field and the pressure oscillations are determined as a root-mean-squared value in a $15ms$ time window centered at the main pressure peak in the Stoneley wave. Figure 9 shows that the electrical fields' amplitudes measured with a $0.5m$ electrode separation, are practically the same as the amplitudes measured with a $1.0m$ electrode separation. Consistency of the electrical field amplitudes measured in different experiments demonstrates that the phenomena observed in the field are repeatable. The electrical field amplitude in Figure 9 is determined as the potential difference between the electrodes

divided by the distance between them. Thus, the $1.0m$ dipoles recorded a potential difference twice that recorded by the $0.5m$ dipoles. This suggests that the recorded signal is not due to the interaction of the Stoneley wave with the electrodes themselves.

Figure 9 also shows the phase shift between the Stoneley-wave-induced electrical fields and the pressure oscillations. The phases of both the pressure and the electrical field oscillations were determined by Fast Fourier Transformation in a cosine-tapered $50ms$ time window centered at the main pressure peak. The values plotted in Figure 9 are averages of phase shifts at different frequencies in an interval from $100Hz$ to $200Hz$, where most of the Stoneley wave energy is concentrated. In granite around the depth of $110m$ and in diorite (below $140m$) phase shifts estimated at different frequencies were not consistent with each other, due to a low signal-to-noise ratio. To indicate that at these depth the average value is not a reliable estimate of the phase shift, we plotted it using a dashed line.

Comparison of Figure 9 with Figures 3 and 4 shows that the amplitude of the electrical signal is high in fractured zones (zones of high P-wave slowness and conductivity in Figure 4) and low in unfractured zones. Therefore, the Stoneley-wave-induced electrical fields can be used to detect fractured zones intersecting a borehole.

Electromagnetic Radiation Caused by a Stoneley Wave

Electrical data in Figure 7 show an electrical signal which arrived simultaneously at all the dipoles at $46ms$ (event B-B). As was mentioned above, the electrical data were recorded 4 traces at a time. Event B-B was consistently recorded at the same time by electrodes placed at different depths in different experiments. Therefore, this signal cannot be attributed to noise (which changes from one group of 4 electrical traces to another).

Signal B-B originated at the time when the direct Stoneley wave encountered a fractured zone at the depth of $60m$. Analysis of the amplitude of the signal shows that it decreases away from the depth of $60m$. The simultaneous arrival time means that the signal traveled with the electromagnetic wave velocity. We suggest that this signal is an electromagnetic wave radiated by the Stoneley-wave-induced streaming current within the fractured zone at the depth of $60m$.

THEORETICAL MODEL FOR THE ELECTRICAL FIELD INDUCED BY A STONELEY WAVE

The phenomenon detected most clearly and repeatedly in our experiment is the electrical field induced by the Stoneley wave. The amplitude of this electrical field is high in fractured zones and low in unfractured rock. To determine what specific characteristic of fractured zones can be deduced from the amplitude and the phase of the Stoneley-wave-induced electrical field, we developed the following theoretical model.

A Stoneley wave of frequency ω propagating with a phase velocity $c_s(\omega)$ downward in a borehole drilled through a homogeneous porous formation, induces oscillations of

fluid pressure P_b in the borehole:

$$P_b(r,z,t) = P_0 \frac{I_0\left(r\frac{\omega}{c_s}\right)}{I_0\left(R_b\frac{\omega}{c_s}\right)} \exp\left(-i\omega t + i\frac{\omega}{c_s}z\right). \quad (1)$$

Here r and z are the cylindrical coordinates (z-axis is pointing down), t is time, and R_b is the borehole radius. The Stoneley wave phase velocity $c_s(\omega)$ is in general a complex number (thus accommodating attenuation). In our experiment, the Stoneley wave's amplitude did not decrease significantly while the wave traveled along the borehole, except where part of the wave energy was reflected upwards by large fractures. Therefore, for the first-order analysis, we can neglect the attenuation, and consider c_s to be real-valued and equal to the apparent phase velocity of the Stoneley wave.

The pore pressure oscillation created in the formation by the Stoneley wave is (Tang *et al.*, 1991)

$$P_f(r,z,t) = P_0 \frac{K_0\left(r\sqrt{-\frac{i\omega}{D}+\left[\frac{\omega}{c_s}\right]^2}\right)}{K_0\left(R_b\sqrt{-\frac{i\omega}{D}+\left[\frac{\omega}{c_s}\right]^2}\right)} \exp\left(-i\omega t + i\frac{\omega}{c_s}z\right), \quad (2)$$

where D is the pore-fluid dynamic diffusivity. In Equations 1 and 2, I_0 and K_0 are the zero-order modified Bessel functions.

The pore pressure gradient, induced in the formation by the Stoneley wave, causes a flow of an ion-carrying pore fluid, and results in a streaming electrical current. Thus, total electrical current density is the sum of the conductive current and streaming current densities:

$$\underline{j}_{total} = \underline{j}_{conductive} + \underline{j}_{streaming} = \sigma_r \underline{E} + L\nabla P_f. \quad (3)$$

Here $\underline{E}$ is the electrical field vector, σ_r is the formation conductivity, and L is the streaming current coupling coefficient, given by Pride (1994):

$$L = \frac{\phi_{ic}}{\alpha_\infty}\frac{\zeta\epsilon_f}{\mu}\left[1-\frac{i\omega}{\omega_c}\right]^{-\frac{1}{2}}, \quad (4)$$

where ϕ_{ic} is the interconnected porosity, α_∞ is the pore space tortuosity, ζ is the zeta-potential (determined by the electrochemical interaction between the pore fluid and the rock), ϵ_f is the pore fluid permittivity, μ is the pore fluid viscosity, and ω_c is the critical frequency for the formation (fractured zone). The Biot theory determines ω_c as the frequency which separates the viscosity-dominated flow regime from the inertia-dominated flow regime. Equation 4 states that for the viscosity-dominated flow regime ($\omega << \omega_c$) the coupling coefficient does not change with frequency, and for the inertia-dominated flow regime ($\omega >> \omega_c$) the coupling coefficient decreases as $\left[\frac{\omega}{\omega_c}\right]^{-\frac{1}{2}}$. The Biot critical frequency for the formation is (Johnson *et al.*, 1987)

$$\omega_c = \frac{\phi_{ic}\mu}{\alpha_\infty \rho_f k_0}\cdot\frac{2}{M}, \quad (5)$$

where k_0 is the formation static permeability, ρ_f is the pore fluid density, and the parameter M is close to 1 for most media.

The combination of Equations 2, 3 and 4 leads to an analytical solution for the vertical component of the electrical field in the borehole:

$$\frac{E_z}{P_b} = \frac{\frac{\phi_{ic}}{\alpha_\infty}\frac{\zeta\epsilon_f}{\mu}\left[-\frac{i\omega}{c_s}\right]\left[1-\frac{i\omega}{\omega_c}\right]^{-\frac{1}{2}}}{\sigma_r + \sigma_f \frac{I_1\left(R_b\frac{\omega}{c_s}\right)}{I_0\left(R_b\frac{\omega}{c_s}\right)}\frac{K_0\left(R_b\frac{\omega}{c_s}\right)}{K_1\left(R_b\frac{\omega}{c_s}\right)}}, \tag{6}$$

where σ_f is the pore fluid conductivity. Details of the derivation of Equation 6 are given in the appendix.

If the wavelength of the Stoneley wave is much greater than the borehole radius $\left(R_b\frac{\omega}{c_s} << 1.0\right)$, then Equation 6 can be simplified as

$$\frac{E_z}{P_b} = \frac{\frac{\phi_{ic}}{\alpha_\infty}\frac{\zeta\epsilon_f}{\mu}\left[-i\frac{\omega}{c_s}\right]\left[1-\frac{i\omega}{\omega_c}\right]^{-\frac{1}{2}}}{\sigma_r + \sigma_f\left[R_b\frac{\omega}{c_s}\right]^2\frac{1}{2}\log\left(\frac{2c_s}{R_b\omega}\right)}. \tag{7}$$

Equation 7 gives the amplitude and phase of the electrical field induced by a Stoneley wave forcing a flow of the ion-carrying pore fluid within the permeable formation around the borehole. It is the central result of our theoretical analysis.

COMPARISON OF THE FIELD DATA AND THE THEORY

To test the validity of the theoretical model, we compare the amplitude and phase of the Stoneley-wave-induced electrical field observed in the field with the prediction of Equation 7. It is possible to make such a comparison for the granite section of the well (top $140m$) because all the parameters in Equation 7 are known from independent field and laboratory measurements. In addition, the signal-to-noise ratio of the electrical signals is highest in the granite section.

Table 1 shows the values for the parameters in Equation 7 used for amplitude comparison. The Stoneley wave frequency ω and velocity c_s were determined from the hydrophone measurements (Figure 5). Borehole diameter R_b is taken from the caliper log (Figure 3). The value for the fluid conductivity σ_f corresponds to a salinity of $0.01mol/l$, measured for a sample of the actual borehole fluid (water). The values of the fluid viscosity μ and permittivity ϵ_f are the values for water. The pore space tortuosity α_∞ was assumed to be close to 1.0 for fractures. For the borehole fluid properties in our experiments (salinity of $0.01mol/l$ and $pH = 7.5$), the value of the zeta-potential ζ for granite was taken from laboratory experiments (Ishido and Mizutani, 1981; Morgan *et al.*, 1989; Pride and Morgan, 1991). For a granite formation with a conductivity σ_r of $0.015S/m$ (an average value in granite in Figure 4), and an interconnected porosity ϕ_{ic} of 1% (a reasonable value for fractured granite), Equation 7 predicts the amplitude of the Stoneley-wave-induced electrical field to be $\left|\frac{E_z}{P_b}\right| = 12nV/(m\cdot Pa)$, assuming that

$\omega << \omega_c$. This value of the amplitude is in agreement with the field measurements (Figure 9).

Equation 7 further predicts a (-90^o) phase shift between the electrical field and the pressure oscillations. Figure 9 shows that that in the granite section the phase shift in the field data is around (-90^o). Thus, the theory presented in this paper correctly predicts both the amplitude and the phase of the field data.

INTERPRETATION OF THE FIELD DATA BASED ON THE THEORETICAL MODEL

In this section, we analyze the field data and the analytical solution (Equation 7) for the amplitude and phase of the Stoneley-wave-induced electrical fields to determine what specific information about the formation can be deduced from borehole electroseismic measurements.

Estimating Interconnected Porosity From the Electroseismic Data

If the frequency of the Stoneley wave is less than the Biot critical frequency of the formation ($\omega << \omega_c$), then the interconnected porosity of the formation can be determined from Equation 7 as

$$\phi_{ic} = \left|\frac{E_z}{P_b}\right| \frac{\alpha_\infty \mu}{\zeta \epsilon_f} \frac{c_s}{\omega} \left[\sigma_r + \sigma_f \left[R_b \frac{\omega}{c_s}\right]^2 \frac{1}{2} \log\left(\frac{2c_s}{R_b \omega}\right)\right]. \tag{8}$$

To derive an estimate of the interconnected porosity for the granite section (top $140m$) using Equation 8, we use the values of the electrical field's amplitude, $\left|\frac{E_z}{P_b}\right|$, from Figure 9, and the formation conductivity σ_r from Figure 4. All the other parameters in Equation 8 are independent of depth and are given in Table 1. Figure 10 presents the porosity estimate for the granite section obtained using Equation 8 and a plot of the number of fractures per meter derived from a borehole video log. A visual comparison shows that the two curves correlate.

Electroseismic measurements suggest that, on the average, fracture porosity in granite is decreasing with depth. The borehole video log, however, shows that the number of visible fractures per meter on the average stays the same (Figure 10). To account for this discrepancy, the average fracture aperture has to decrease with depth. The borehole video log shows that the fractures intersecting the borehole are close to horizontal. It is possible that the overburden pressure forces deeper fractures to close more, resulting in a decrease of the fracture aperture with depth.

Correlation of Electroseismic Signals' Amplitude With Lithology

Figure 9 shows that the amplitude of the Stoneley-wave-induced electrical field is a factor of 5 higher in granite (top $140m$) than in diorite ($160m$-$290m$). The simplest

explanation of this observation is that there are less fractures in diorite than in granite. Smaller number of fractures results in lower porosity, and according to Equation 7, the Stoneley wave induces weaker electrical fields in diorite. The borehole video, P-wave slowness, and the conductivity logs also suggest that the fracture porosity in diorite is lower than in granite, thus supporting the above explanation.

However, there is another explanation to this observation. Analysis of the mineral composition of cuttings from the borehole shows that the diorite contains significantly less quartz than the granite. It is possible that due to the lower quartz content, the zeta-potential ζ is lower in diorite than in granite, and therefore the electrokinetic coupling is smaller (Equation 4). Further experiments are necessary to determine zeta-potential values for different rock types in order to separate lithology effects from porosity effects in the field data.

Possibility to Determine Permeability From Electroseismic Measurements in a Wide Frequency Range

Figure 9 shows that the largest isolated fractures intersecting the borehole (depths 210, 255, and $290m$) do not generate significant electroseismic signals, even though their "fracture porosity" is high. It is possible that the electrokinetic coupling in this fractures is low, because the frequency of the Stoneley wave in our experiment is higher than the Biot critical frequency for these fractures (a pressure wave traveling along a fracture is generated). Equation 4 states the electrokinetic coupling decreases above the Biot critical frequency ($\omega >> \omega_c$). This variation of the electrokinetic coupling with frequency provides a possibility to determine the Biot critical frequency and permeability of the formation around the borehole.

Equation 7 shows that for low frequencies ($\omega << \omega_c$) the ratio of the electrical field amplitude to pressure, $\left|\frac{E_z}{P_b}\right|$, increases proportionally to the frequency ω and that the phase shift between the pressure and electrical field oscillations is (-90^o). For high frequencies ($\omega >> \omega_c$), $\left|\frac{E_z}{P_b}\right|$ decreases with frequency as $\omega^{-\frac{3}{2}}$ and the phase shift is (-45^o). Therefore, if electroseismic measurements are made in a wide frequency range, then the Biot critical frequency ω_c could be determined as the frequency at which there is a change in frequency dependence and the phase shift of the electrical signals. Once the Biot critical frequency ω_c is determined, the permeability of the formation k_0 can be estimated from Equation 5 as

$$k_0 = \frac{2\phi_{ic}\mu}{\omega_c \alpha_\infty \rho_f M}. \tag{9}$$

To investigate whether it is feasible to determine permeability from the broad-band electroseismic measurements, we plan further experimental and theoretical work.

COMPARISON OF BOREHOLE ELECTROSEISMIC METHOD WITH STONELEY WAVE ATTENUATION METHODS

The electroseismic method may have advantages over Stoneley wave attenuation methods for detecting and characterizing fractured (permeable) zones. The first advantage is in the sensitivity of the electroseismic method. The analysis of the hydrophone data in Figure 5 shows that the amplitude of the pressure oscillation in the Stoneley wave decreased only by about 20% as the wave traveled from the top of the borehole to the depth of $290m$. At the same time, the amplitude of the electrical field generated by the wave varied by 500% and was highest in the fractured zones. The second advantage of the electroseismic method is that it is not sensitive to borehole washouts, while the Stoneley wave attenuation methods require corrections for variations in borehole geometry. Thus, the sensitivity of the electroseismic borehole measurements to the presence of fractured zones, together with the simplicity of the method, could make it a useful tool for formation evaluation.

CONCLUSIONS

Downhole electroseismic measurements can be used to detect and characterize fractured (permeable) zones intersected by a borehole. The field data and the theoretical model presented in this paper indicate that at a given frequency the amplitude of the electroseismic signals is proportional to the interconnected porosity (provided that the frequency of the Stoneley wave is less than the Biot critical frequency for the fractures). Theoretical analysis also suggests that if electroseismic measurements are performed over a wide frequency range, then the critical frequency for the fractures could possibly be determined, thus providing information about the permeability. The results of this study suggest that the borehole electroseismic method could be developed into a logging or a VSP tool for detecting and characterizing permeable zones around a borehole.

ACKNOWLEDGMENTS

We thank Dr. Art Thompson, Prof. Gary Olhoeft, and Dr. Keith Katahara for their suggestion regarding the design of the field experiment. We are grateful to Prof. Ted Madden, Dr. Dan Burns and Prof. Gene Simmons for their suggestion and help throughout the course of this study. We also thank Mr. Peter Britton of The Riess Institute for his enthusiastic support of our studies, and Dr. Fred Paillet and Hager-Richter Geoscience, Inc. for providing the logs.

This work was supported by the Borehole Acoustics and Logging Consortium at the Massachusetts Institute of Technology.

REFERENCES

Broding, R. A., Buchanan, S. D., and Hearn, D. P., 1963, Field experiments on the electroseismic effect: *IEEE Trans. Geosci. Electronics, GE-1*, 23–31.

Butler, K. E., Russel, R. D., Kepic, A. W., and Maxwell, M., 1996, Measurement of the seismoelectric response from a shallow boundary: *Geophysics, 61*, 1769–1778.

Haartsen, M. W., and Pride, S. R., 1994, Modeling of coupled electroseismic wave propagation from point sources in layered media: 64th Ann. Internat. Mtg., Soc. Expl. Geophys., Expanded Abstracts, 1155–1158.

Haartsen, M. W., 1995, Coupled electromagnetic and acoustic wavefield modeling in poro-elastic media and its applications in geophysical exploration: Ph.D. thesis, Massachusetts Institute of Technology.

Ishido, T., and Mizutani, H., 1981, Experimental and theoretical basis of electrokinetic phenomena in rock-water systems and its applications to geophysics: *J. Geophys. Res., 86*, 1763–1775.

Johnson, D. L., Koplik, J., and Dashen, R., 1987, Theory of dynamic permeability and tortuosity in fluid-saturated porous media: *J. Fluid Mech., 176*, 379–400.

Mikhailov, O. V., Haartsen, M. W., and Toksöz, M. N., 1997, Electroseismic investigation of the shallow subsurface: field measurements and numerical modeling: *Geophysics, 62*, 97–105.

Morgan, F. D., Williams, E. R., and Madden, T. R., 1989, Streaming potential properties of Westerly granite with applications: *J. Geophys. Res., 94*, 12449–12461.

Parkhomenko, E. I., and Gaskarov, I. V., 1971, Borehole and laboratory studies of the seismoelectric effect of the second kind in rocks: *Izv. Akad Nauk SSSR, Physics of the Solid Earth, 9*, 88–92.

Pride, S. R., and Morgan, F. D., 1991, Electrokinetic dissipation induced by seismic waves: *Geophysics, 56*, 914–925.

Pride, S. R., 1994, Governing equations for the coupled electromagnetics and acoustics of porous media: *Phys. Rev. B, 50*, 15678–15696.

Tang, X. M., Cheng, C. H., and Toksöz, M. N., 1991, Dynamic permeability and borehole Stoneley waves: A simplified Biot-Rosenbaum model: *J. Acoust. Soc. Am., 90*, 1632–1646.

Thompson, A. H., and Gist, G. A., 1993, Geophysical applications of electrokinetic conversion: *The Leading Edge, 12*, 1169–1173.

APPENDIX

Solution for the Amplitude and Phase of the Stoneley-Wave-Induced Electrical Field

We start our analysis with a full set of the Maxwell's equations. Comparison of the relative magnitude of the terms in the equations showed that at the frequencies and space-scales of the experiments, the terms containing differentiation with respect to time can be neglected. Thus, the full set of the Maxwell's equations reduces to the quasi-electrostatic equations for a conductive medium:

$$\nabla \cdot \underline{j} = 0 \tag{A-1}$$

$$\nabla \times \underline{E} = 0. \tag{A-2}$$

Our field data shows that at the sensitivity level of the measurements, electromagnetic waves were only detected in rare instances. At the same time, the electrical fields locally induced by a Stoneley wave were very clear in the field data. Therefore, the field data support the validity of neglecting "radiative" terms (i.e., the terms containing differentiation with respect to time) in the Maxwell's equations.

Equation A-2 allows introduction of the electrical potential:

$$\underline{E} = -\nabla\Phi. \tag{A-3}$$

In the fluid filling the borehole, the electrical current density is determined by the fluid conductivity:

$$\underline{j} = \underline{j}_{conductive} = \sigma_f \underline{E}. \tag{A-4}$$

In the formation around the borehole, the electrical current density is a sum of the conductive and streaming current densities:

$$\underline{j} = \underline{j}_{conductive} + \underline{j}_{streaming} = \sigma_r \underline{E} + L\nabla P_f. \tag{A-5}$$

A combination of Equations A-3, A-4 and A-1 gives an equation for the electrical potential in the borehole:

$$\sigma_f \nabla^2 \Phi = 0. \tag{A-6}$$

Similarly, a combination of Equations A-3, A-5 and A-1 gives an equation for the electrical potential in the formation:

$$\sigma_r \nabla^2 \Phi = L\nabla P_f. \tag{A-7}$$

An axisymmetric solution for Equations A-6–A-7, that is finite at $r = 0$ and $r = \infty$ is

$$\Phi = A \cdot \frac{I_0\left(r\frac{\omega}{c_s}\right)}{I_0\left(R_b\frac{\omega}{c_s}\right)} \exp\left(-i\omega t + \frac{\omega}{c_s}z\right), \qquad r < R_b \tag{A-8}$$

$$\Phi = \frac{L}{\sigma_r} P_f + B \cdot \frac{K_0\left(r\frac{\omega}{c_s}\right)}{K_0\left(R_b\frac{\omega}{c_s}\right)} \exp\left(-i\omega t + \frac{\omega}{c_s} z\right), \qquad r > R_b, \tag{A-9}$$

where pressure P is given by Equation 2, and coefficients A and B are to be determined from boundary conditions.

At the borehole wall, the electrical potential and the normal electrical current have to be continuous. These boundary conditions provide two equations for coefficients A and B:

$$A = \frac{L}{\sigma_r} P_0 + B, \tag{A-10}$$

$$-\sigma_f A \frac{\frac{\omega}{c_s} I_1\left(R_b\frac{\omega}{c_s}\right)}{I_0\left(R_b\frac{\omega}{c_s}\right)} = \sigma_r B \frac{\frac{\omega}{c_s} K_1\left(R_b\frac{\omega}{c_s}\right)}{K_0\left(R_b\frac{\omega}{c_s}\right)}. \tag{A-11}$$

Solving Equations A-10 and A-11 results in:

$$A = \frac{LP_0}{\sigma_r + \sigma_f \frac{I_1\left(R_b\frac{\omega}{c_s}\right)}{I_0\left(R_b\frac{\omega}{c_s}\right)} \frac{K_0\left(R_b\frac{\omega}{c_s}\right)}{K_1\left(R_b\frac{\omega}{c_s}\right)}}, \tag{A-12}$$

$$B = -\frac{LP_0}{\sigma_r} + \frac{LP_0}{\sigma_r + \sigma_f \frac{I_1\left(R_b\frac{\omega}{c_s}\right)}{I_0\left(R_b\frac{\omega}{c_s}\right)} \frac{K_0\left(R_b\frac{\omega}{c_s}\right)}{K_1\left(R_b\frac{\omega}{c_s}\right)}}. \tag{A-13}$$

Equations A-8–A-9 and A-12–A-13 give the full solution for the electrical potential in and around the borehole. The vertical component of the electrical field can be obtained according to Equation A-3 by differentiating the expression for the electrical potential with respect to z:

$$E_z = \frac{LP_0\left[-i\frac{\omega}{c_s}\right]}{\sigma_r + \sigma_f \frac{I_1\left(R_b\frac{\omega}{c_s}\right)}{I_0\left(R_b\frac{\omega}{c_s}\right)} \frac{K_0\left(R_b\frac{\omega}{c_s}\right)}{K_1\left(R_b\frac{\omega}{c_s}\right)}} \frac{I_0\left(r\frac{\omega}{c_s}\right)}{I_0\left(R_b\frac{\omega}{c_s}\right)} \exp\left(-i\omega t + i\frac{\omega}{c_s}\right). \tag{A-14}$$

Finally, dividing Equation A-14 by Equation 1 gives the ratio of the electrical field to pressure in the borehole:

$$\frac{E_z}{P_b} = \frac{L\left[-i\frac{\omega}{c_s}\right]}{\sigma_r + \sigma_f \frac{I_1\left(R_b\frac{\omega}{c_s}\right)}{I_0\left(R_b\frac{\omega}{c_s}\right)} \frac{K_0\left(R_b\frac{\omega}{c_s}\right)}{K_1\left(R_b\frac{\omega}{c_s}\right)}}. \tag{A-15}$$

This equation is a solution for general L. If L is expressed in terms of the rock properties (e.g. Equation 4), then the solution for the amplitude and phase of the Stoneley-wave-induced electrical field is complete.

Parameter	Value
Stoneley wave frequency ω	$2\pi \cdot 150Hz$
Stoneley wave velocity c_s	$1400m/s$
borehole radius R_b	$0.15m$
fluid conductivity σ_f	$0.12S/m$
fluid viscosity μ	$10^{-3}Pa \cdot s$
fluid permittivity ϵ_f	$7.1 \cdot 10^{-10}coul^2/(N \cdot m^2)$
formation tortuosity α_∞	1
zeta potential ζ	$-40mV$

TABLE 1. Parameters of the experiment used for amplitude comparison and for estimating the interconnected porosity.

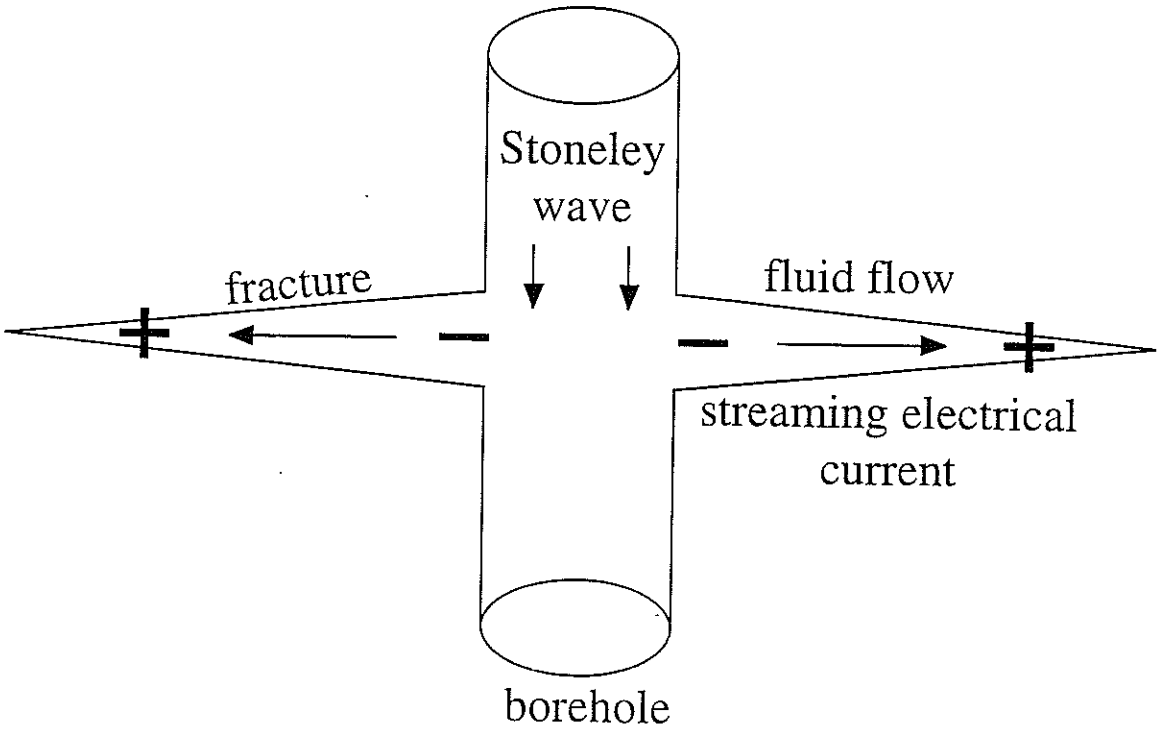

Figure 1: Diagram of a Stoneley wave inducing an electrical field. When a Stoneley wave travels past a fractured zone, it forces a flow of ion-carrying pore fluid within the fractures, thus generating a streaming electrical current. This current results in a time-varying charge separation, which induces an electrical field.

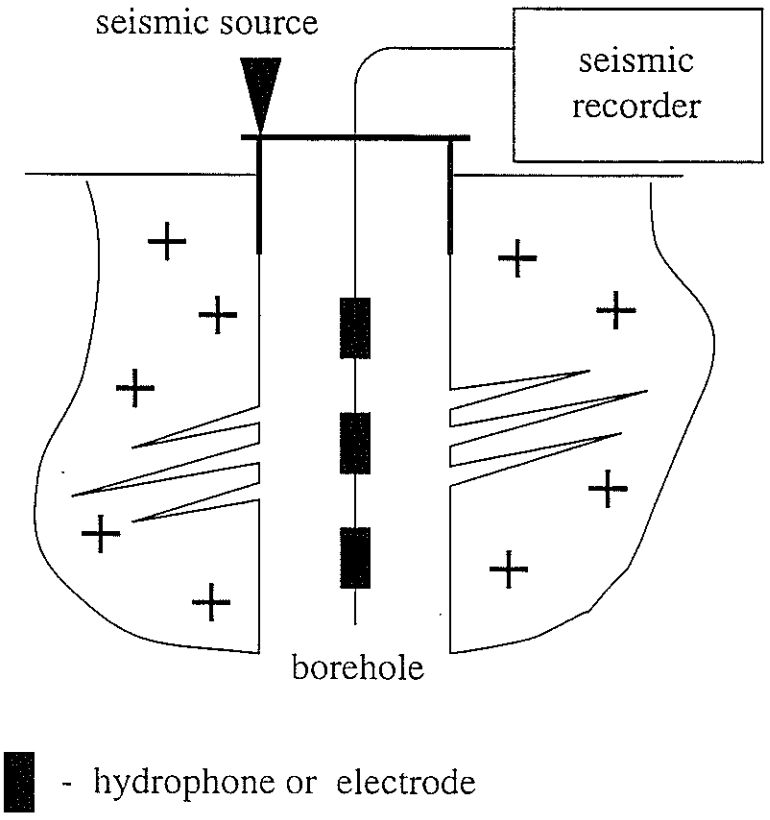

Figure 2: Diagram of the experimental setup.

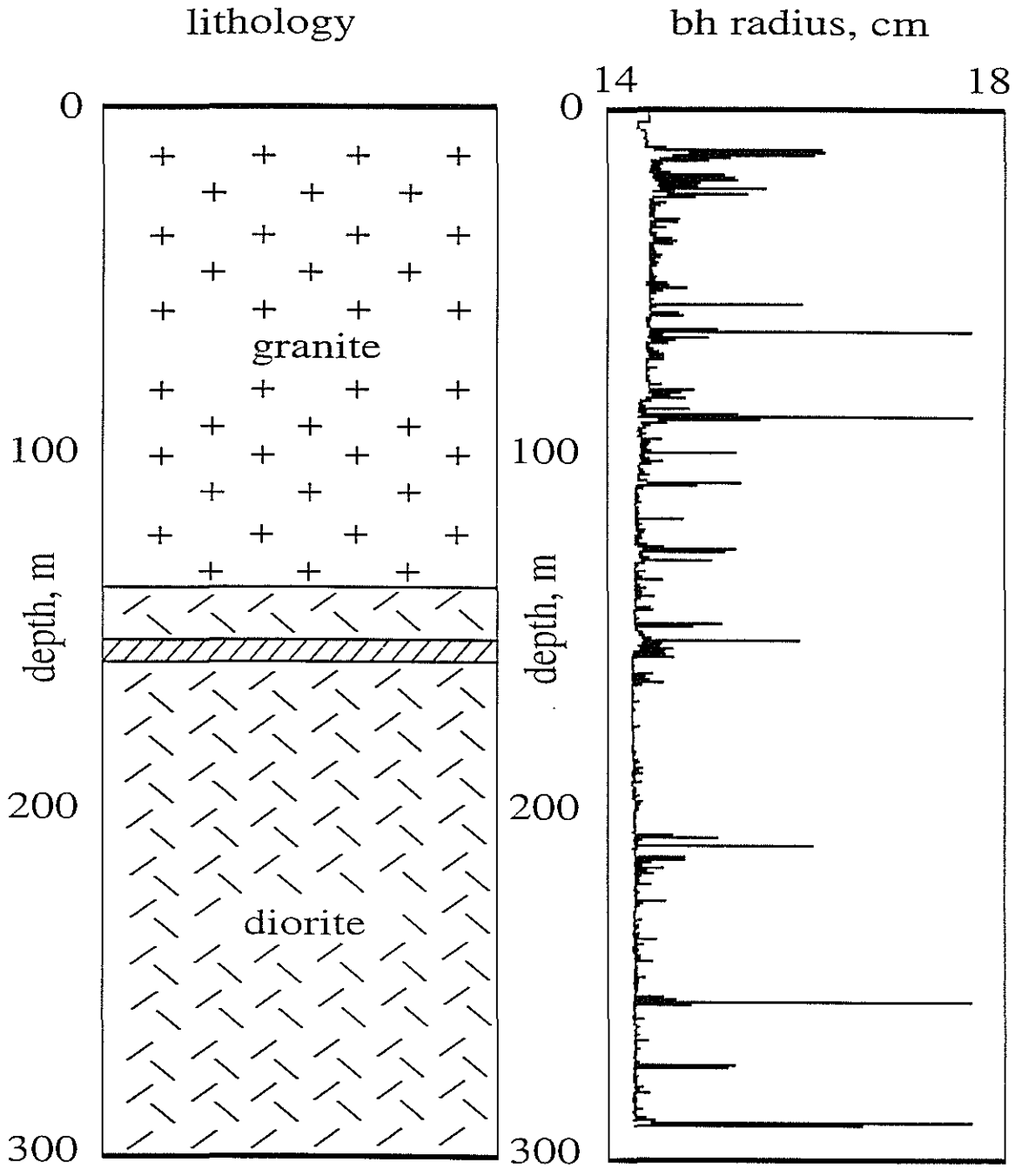

Figure 3: Lithological description of the formation and the borehole caliper log.

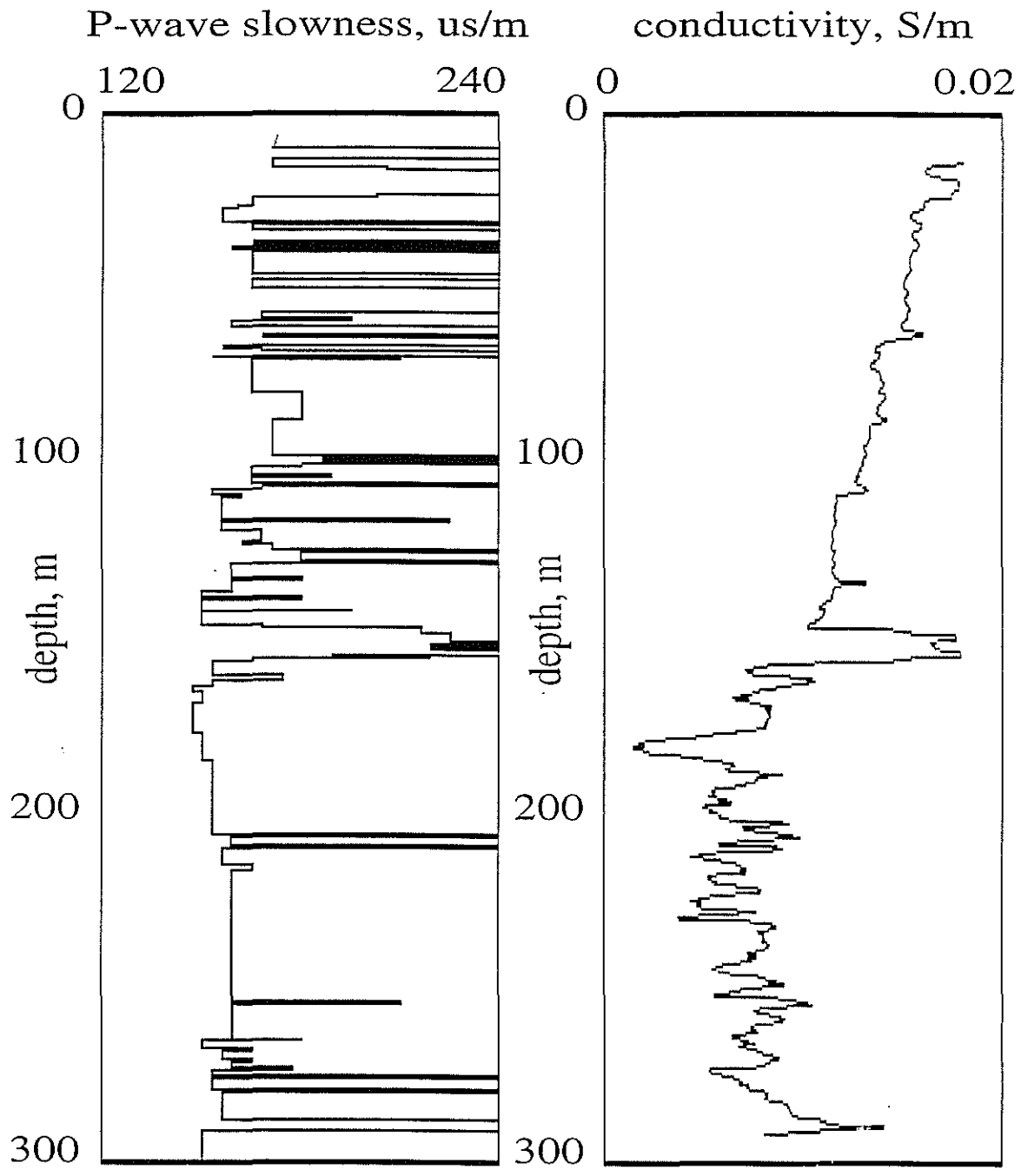

Figure 4: P-wave slowness and conductivity logs for the formation.

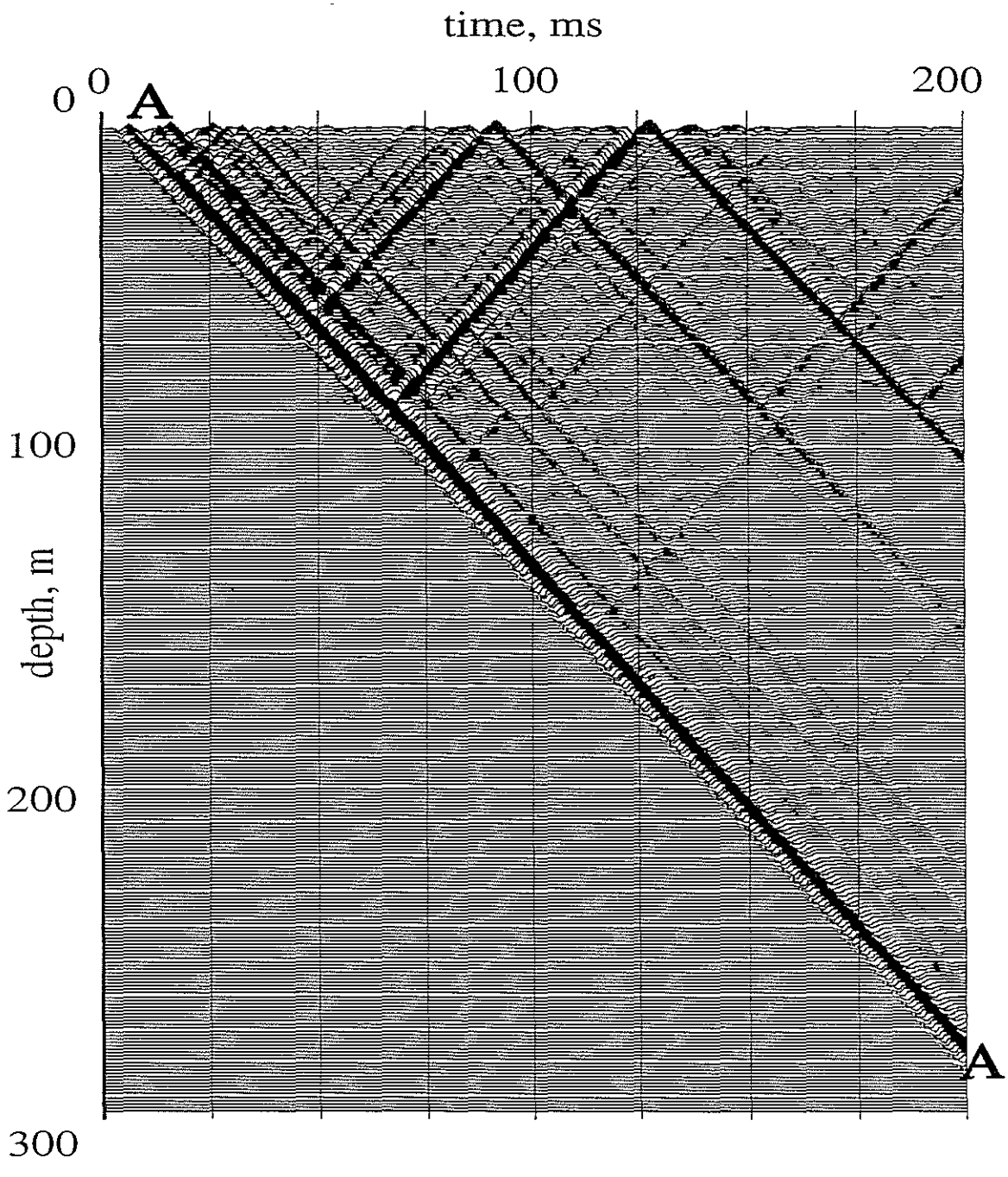

Figure 5: Hydrophone measurements. Event A-A is the direct Stoneley wave.

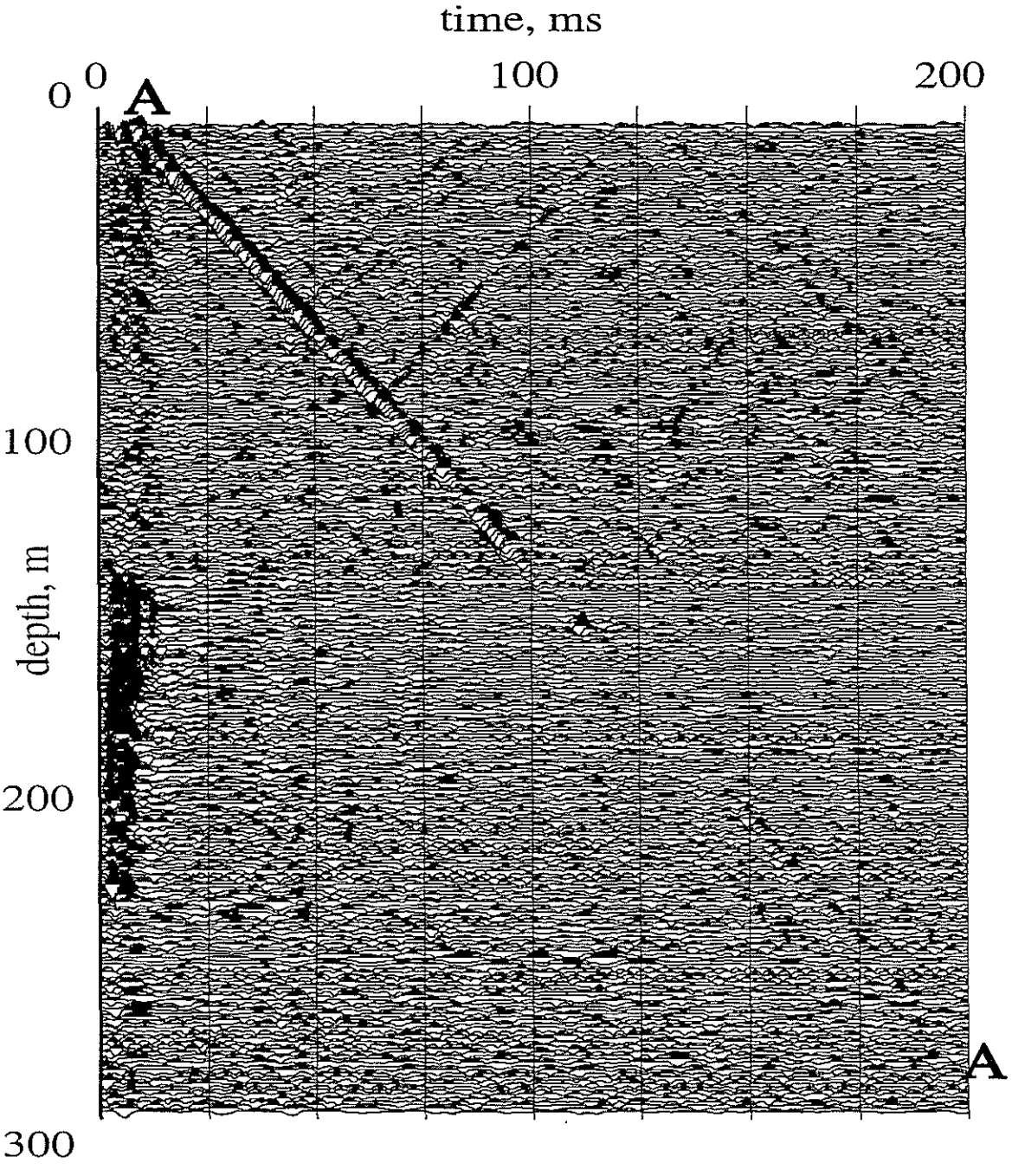

Figure 6: Electrical measurements made with $0.5m$ electrode separation. Event A-A is the electrical field induced by the direct Stoneley wave.

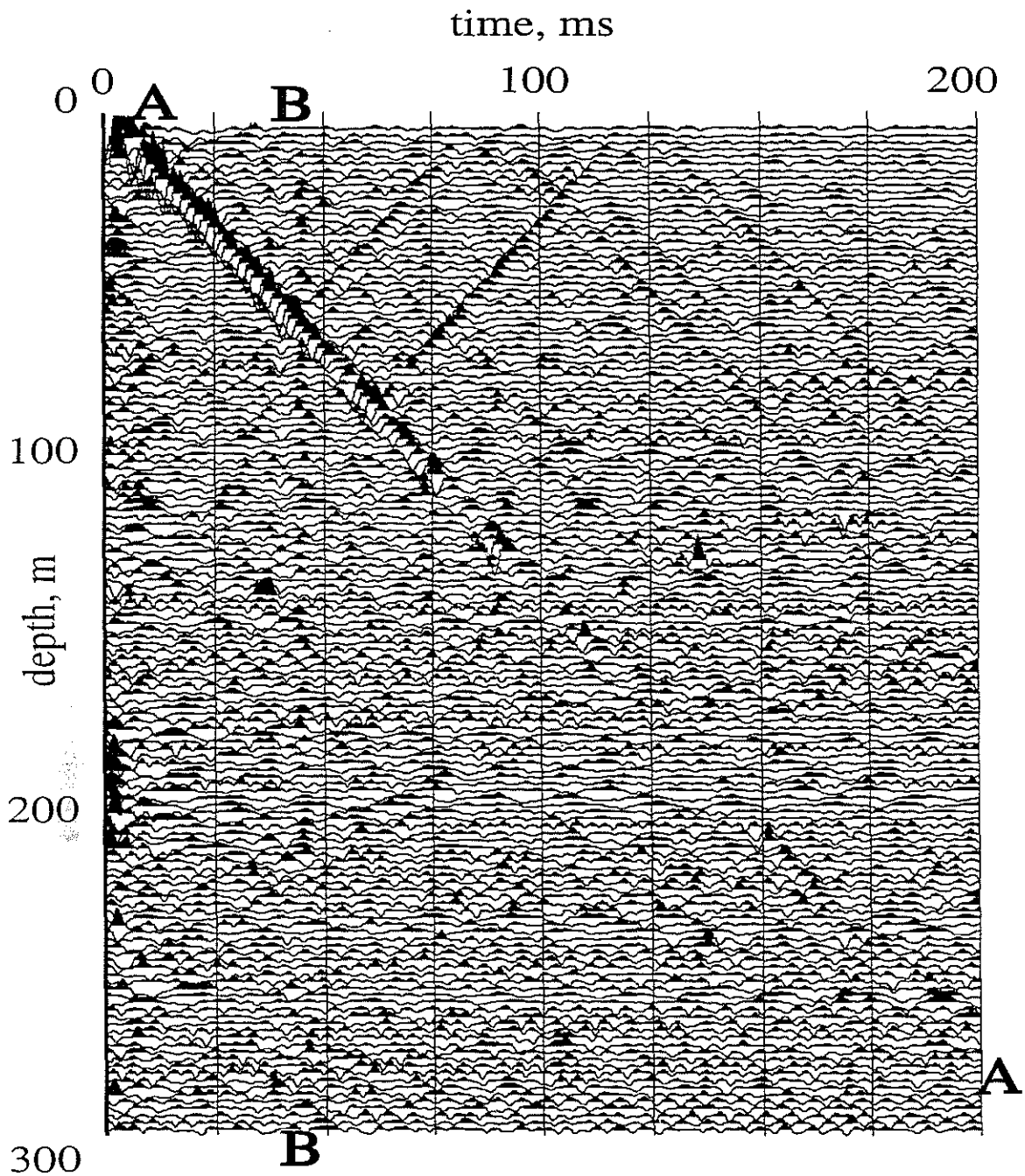

Figure 7: Electrical measurements made with $1.0m$ electrode separation. Event A-A is the electrical field induced by the direct Stoneley wave. Event B-B is the electromagnetic wave radiated by the Stoneley-wave-induced electrical current within the fractured zone at the $60m$ depth.

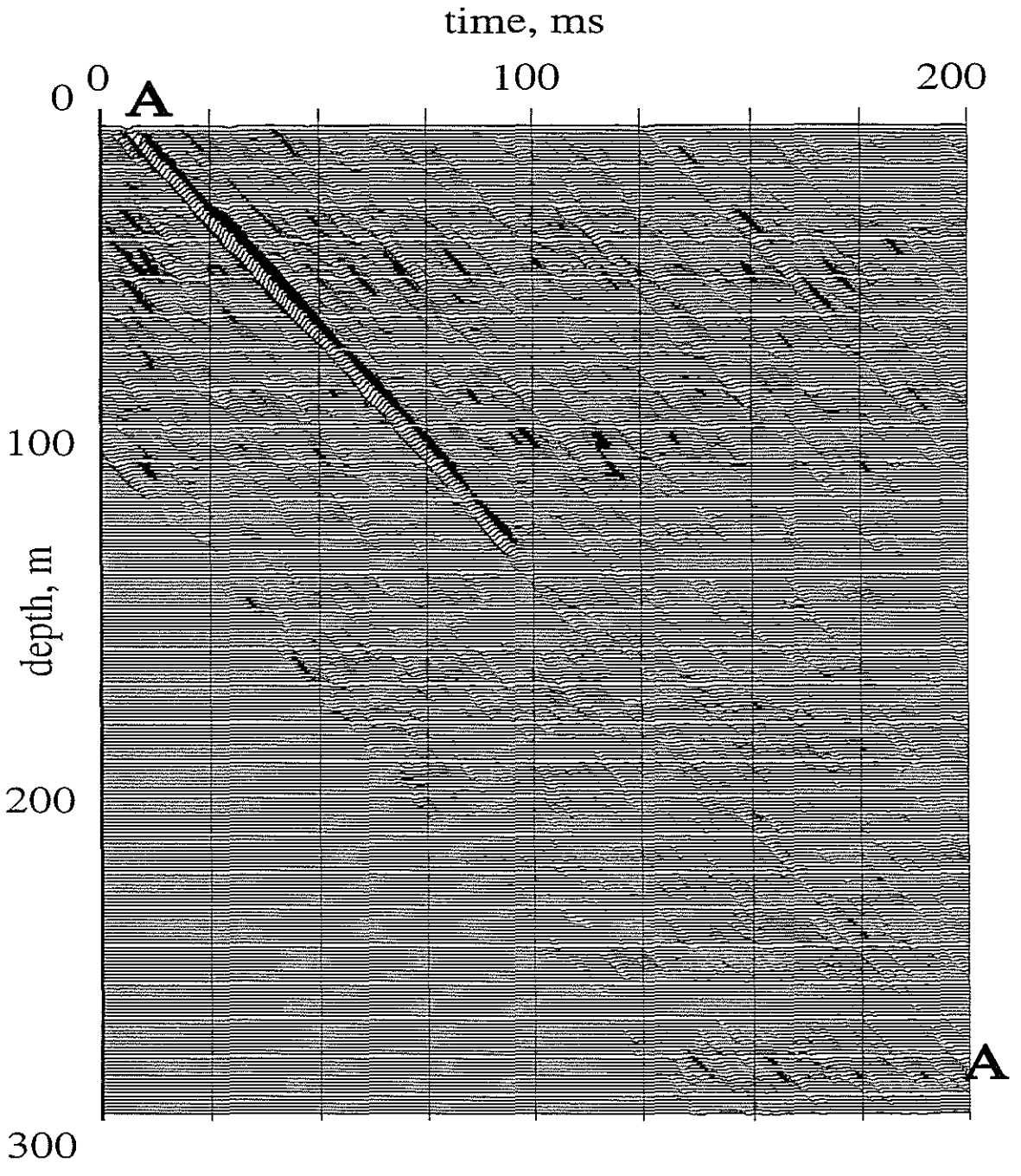

Figure 8: Electrical data from Figure 6 median-filtered to enhance the electrical field induced by the direct Stoneley wave (Event A-A).

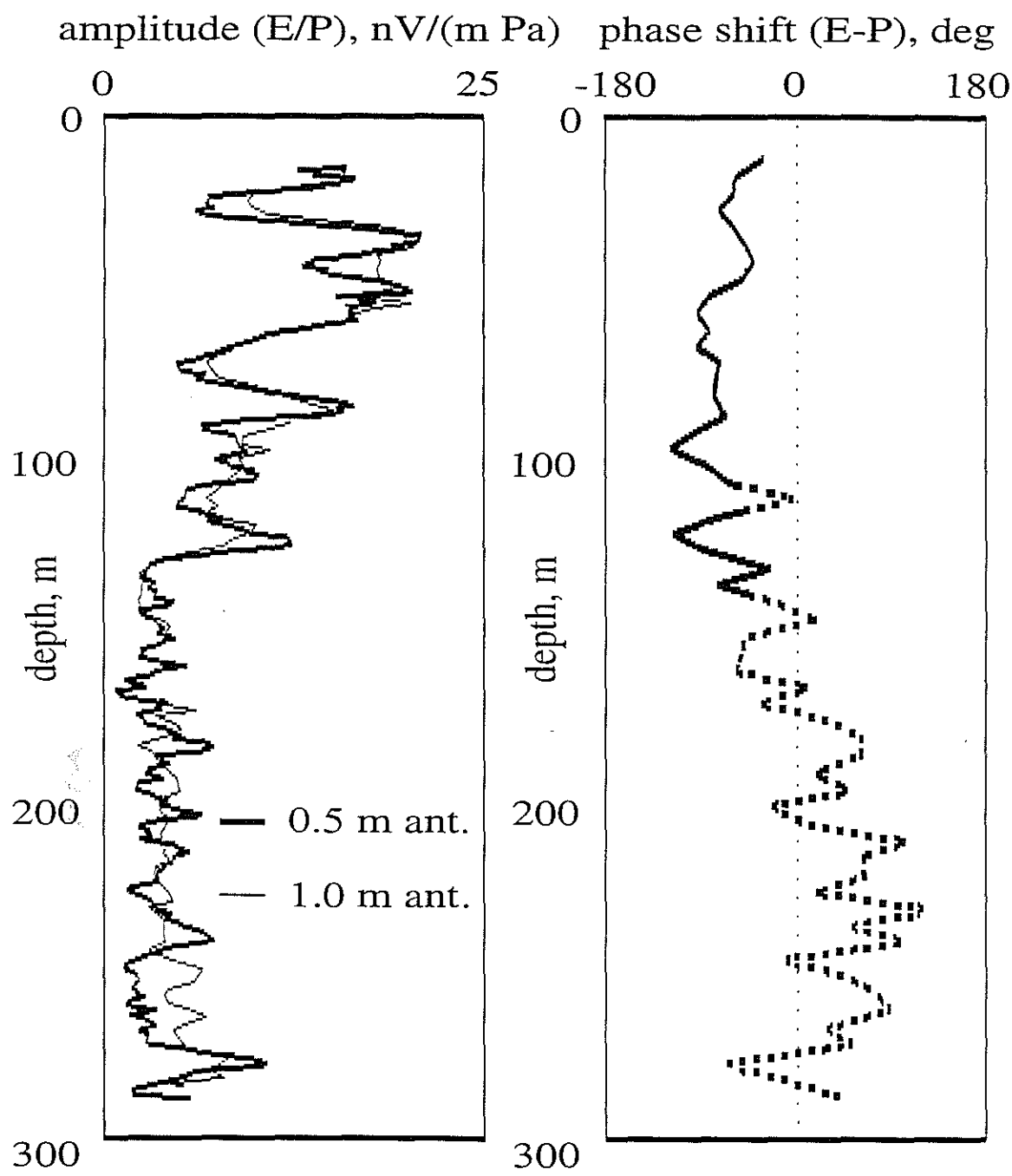

Figure 9: Amplitude of the Stoneley-wave-induced electrical field normalized by pressure, and the phase shift between the electrical field and pressure oscillations. Amplitude and phase of the Stoneley-wave-induced electrical field measured in the experiment agree with predictions of Equation 7.

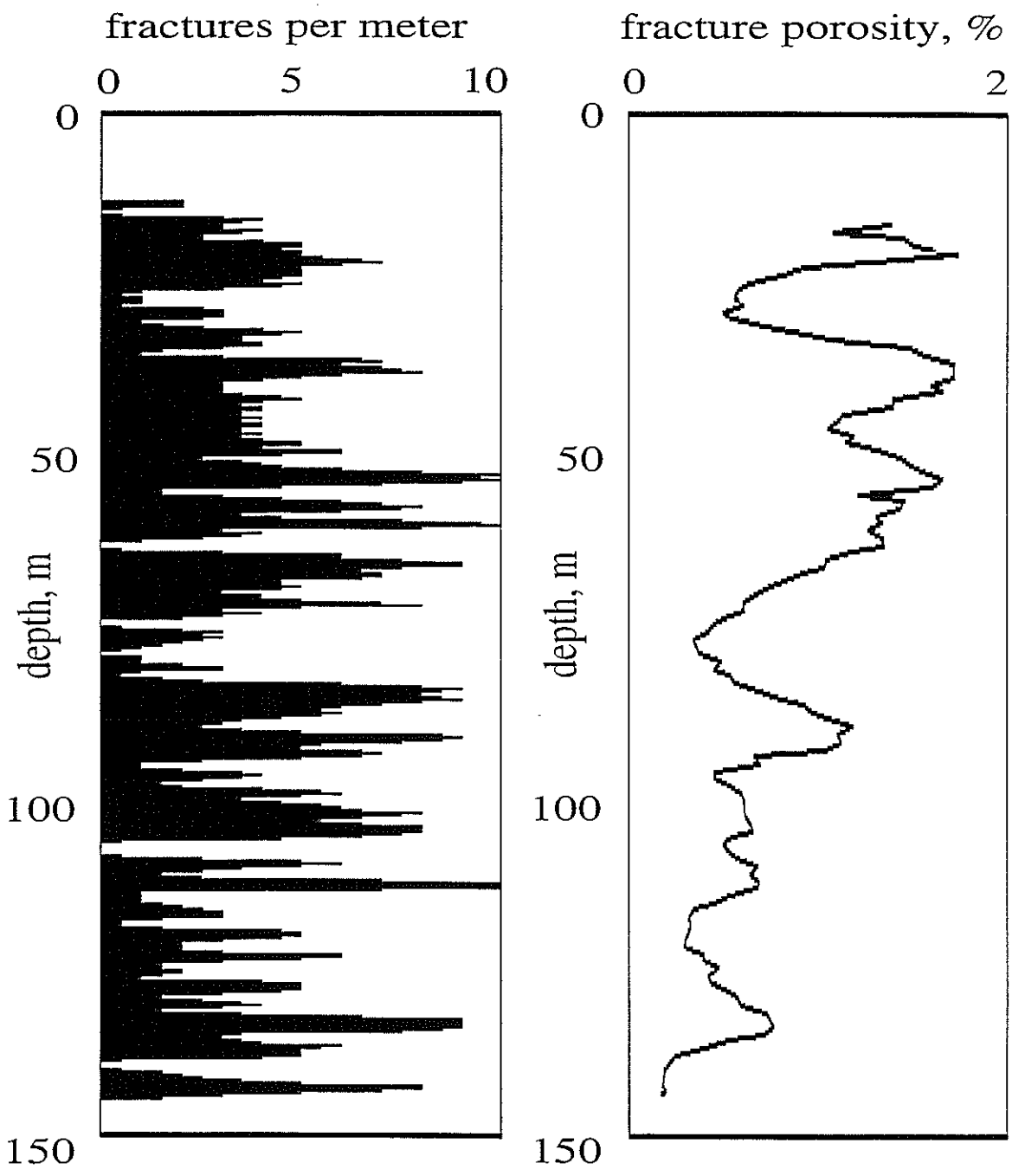

Figure 10: Interconnected porosity estimate derived from the electroseismic field data, and a fracture density log derived from the borehole video.